Spatial analysis reveals distinct immune phenotypes and tertiary lymphoid structure-like aggregates in pediatric acute myeloid leukemia

Joost B. Koedijk[1,2], Inge van der Werf[1], Marijn A. Vermeulen[1], Alicia Perzolli[1,2], Marta Fiocco[1,3,4], Hester A. de Groot-Kruseman[1], Rubina Moeniralam[1], Stefan Nierkens[1,5], Mirjam E. Belderbos[1], C. Michel Zwaan[1,2#], Olaf Heidenreich[1,6#]

[1]Princess Máxima Center for Pediatric Oncology, 3584 CS Utrecht, The Netherlands.

[2]Department of Pediatric Oncology, Erasmus MC/Sophia Children's Hospital, 3015 GD Rotterdam, The Netherlands.

[3]Mathematical Institute, Leiden University, Leiden, The Netherlands

[4]Department of Biomedical Data Sciences, Leiden University Medical Center, Leiden, The Netherlands.

[5]Center for Translational Immunology, University Medical Center Utrecht, 3584 CX Utrecht, The Netherlands.

[6]Wolfson Childhood Cancer Research Centre, Newcastle University, Newcastle upon Tyne NE1 7RU, UK.

[#]Equal contribution

Abstract

Pediatric cancers are characterized by a relatively low mutational burden and therefore, children are thought to be poor candidates for T cell-engaging immunotherapies. Here, we performed a multidimensional characterization of the tumor immune microenvironment in newly diagnosed children with acute myeloid leukemia (AML) and non-leukemic controls. We identified a subset of pediatric AML patients with remarkably high levels of T cell infiltration and a relatively low abundance of anti-inflammatory macrophages. In addition, we detected large T cell networks that colocalized with B cells in the bone marrow of immune-infiltrated samples, resembling tertiary lymphoid structures as described in solid tumors. Using spatial transcriptomics, we dissected the composition of these structures and revealed unique hotspots of anti-tumor immunity. This work raises the possibility that a subset of pediatric AML patients may benefit from T cell-engaging immunotherapies and encourages further study of these lymphoid structures in the context of immunotherapy in AML.

Lead contacts: Joost B. Koedijk & Olaf Heidenreich, Princess Máxima Center for Pediatric Oncology, 3584 CS Utrecht, The Netherlands. Phone: 088-9727272; E-mail: j.b.koedijk@prinsesmaximacentrum.nl & o.t.heidenreich@prinsesmaximacentrum.nl

Running title: The spatial immune landscape of pediatric AML

Disclosure of conflicts of interest: The authors declare no financial conflicts of interest.

Keywords: spatial transcriptomics, digital spatial profiling, bone biopsy, secondary lymphoid organs, ectopic, T cell networks, hematological malignancies, children.

A tumor microenvironment that is infiltrated by cytotoxic T cells is of crucial importance to elicit a response to T cell-engaging immunotherapies such as immune checkpoint inhibitors and bispecific antibodies (Bruni, Angell & Galon, 2020). In contrast, patients with an immune-depleted or 'cold' tumor microenvironment show significantly reduced response rates. Due to the relatively low mutational burden and the associated poor immunogenicity of pediatric cancers, children are thought to be poor candidates for immunotherapy (Majzner et al., 2017; Pfister et al., 2022). Among pediatric cancers, pediatric acute myeloid leukemia (AML) is a cancer with a particularly low mutational burden (Gröbner et al., 2018). Nonetheless, recent evidence suggests that considerable variation in immune cell infiltration exists among cancers that are considered to be immunologically 'cold' (Dufva et al., 2020; Serroukh et al., 2023; Daver et al., 2021). For instance, in adult AML, which has a relatively low mutational burden in comparison to other adult cancer types, *TP53* mutations have been linked to relatively high immune cell infiltration in the bone marrow (BM) and improved responses to immunotherapy in comparison to *TP53*-WT adult AML (Gröbner et al., 2018; Dufva et al., 2020; Vadakekolathu et al., 2020). However, little is known about the immune compartment in the BM of pediatric AML patients and clinical trials that evaluate the efficacy of such therapies have only recently been initiated for this population (Koedijk et al., 2021). Therefore, it is unclear whether children with AML may be successfully treated with T cell-engaging immunotherapies. This prompted us to perform a multidimensional characterization of the tumor immune microenvironment in newly diagnosed children with *de novo* AML and non-leukemic controls. We identify a subset of patients with remarkably high T cell infiltration in the BM, dissect the spatial immune organization and specifically, unravel the composition of tertiary lymphoid structure-like aggregates in the BM of AML, with implications for future immunotherapy approaches.

Results

A subset of pediatric AML patients has remarkably high T cell infiltration in the bone marrow

For this study, we obtained 53 formalin-fixed and paraffin-embedded (FFPE) bone biopsies from a representative cohort of pediatric patients with treatment-naïve *de novo* AML (n=43), and from age- and sex-matched pediatric patients with treatment-naïve early-stage rhabdomyosarcoma without evidence of malignancy infiltrating the BM (non-leukemic controls, n=10; **Fig. 1A**). Patient characteristics are depicted in **Extended Data Table 1**. Using immunohistochemistry (IHC), we found a decreased abundance of both the overall number of T cells and cytotoxic T cells in pediatric AML patients in comparison to non-leukemic controls (representative images are shown in **Fig. 1B-C**; two-sided P = 0.006 and P = 0.003, respectively; **Fig. 1D-E**). However, the extent of overall T cell and cytotoxic T cell infiltration

could differ up to 90-fold between individual AML patients, with several patients showing relatively high T cell infiltration in the BM**.** Because it has previously been shown that cancer cells' genetic alterations may shape the tumor immune microenvironment, we assessed if certain AML-associated genetic alterations were linked to the level of T cell infiltration (Wellenstein & De Visser, 2018). Interestingly, most of the patients with relatively high T cell infiltration in the BM had *KMT2A*-rearranged AML, the most common cytogenetic abnormality in pediatric AML, although there was wide variation among this cytogenetic subgroup (De Rooij, Zwaan & Van den Heuvel-Eibrink, 2015). In contrast, most other cytogenetic groups showed low levels of both populations with little variation between patients, although several outliers were seen in these groups as well (**Fig 1F-G**). Collectively, we identified substantial variation in T cell infiltration in the BM of pediatric AML with a subset of patients showing a remarkably high T cell frequency in the BM.

Immune infiltrated leukemias are characterized by tumor-specific T cell responses and a relatively low abundance of anti-inflammatory macrophages

To further study pediatric AML patients with a relatively high T cell abundance in the BM, we dichotomized patients into immune-infiltrated (n=8) and immune-depleted (n=35) groups using the non-leukemic controls' median value of cytotoxic T cells as the cut-off value. Subsequently, we performed immune-related gene expression profiling on a cytogenetically representative subset of immune-infiltrated (n=5) and immune-depleted (n=18) samples. Among this subset, four out of five (80%) immune-infiltrated samples had a KMT2A-rearrangement, while five out of eighteen (28%) samples in the immune-depleted group had this cytogenetic abnormality (**Extended Data Table 1**). First, we focused on cytotoxicity-related- and immune checkpoint genes since their expression may give insight into the likelihood of response to immune checkpoint inhibitors. In our cohort, immune-infiltrated patients showed upregulation of both cytotoxic T cell genes (*CD8A*, *CD8B*) and cytotoxicity-related genes including *GZMK*, suggestive of enrichment of $GZMK^+$ cytotoxic T cells, which has been associated with response to PD-1 blockade in adult AML patients (**Fig. 2A**; Abbas et al., 2021). Moreover, pediatric AML patients with an immune-infiltrated BM highly expressed *TNFRSF9* (encoding CD137) and the immune checkpoint genes *PDCD1* (encoding PD-1), *CTLA4*, *TIGIT* and *LAG3,* indicative of tumor-specific T cell responses that may be successfully reinvigorated by ICIs (Ye et al., 2014; Philip & Schietinger, 2022; **Fig. 2A**). Importantly, using a publicly available pediatric AML scRNAseq dataset, we confirmed that the above-mentioned checkpoint genes are mainly expressed by cytotoxic T cells, and that *TIGIT* and *LAG3* were the most widely expressed among this population (n=8 patients; Bailur et al., 2020; **Extended Data Fig. 1A-E**). Taken together, these results suggest that pediatric AML patients with an immune-infiltrated BM may show increased responses to immune checkpoint inhibitors in

comparison to patients with an immune-depleted BM, and that the immune checkpoints TIGIT and LAG-3 may prove suitable targets to enhance cytotoxic T cell function in pediatric AML.

We next investigated whether we could identify differences in factors that either promote or restrict T cell infiltration in the BM. As anticipated, immune-infiltrated samples had significantly higher expression of genes related to T cell-attracting chemokines (*CXCL9*, *CXCL10*), and their corresponding receptor (*CXCR3*; **Fig. 2A**). In line with this, pathway analysis using GO biological processes indicated that immune-infiltrated samples were enriched in T cell migratory and -chemotaxis pathways, suggesting that immune-depleted samples are devoid of signals that attract T cells to the BM (**Fig. 2B**). From solid cancers, we know that macrophages in the tumor microenvironment are the main regulators of the extent of T cell infiltration into the tumor (House et al., 2020; Hoch et al., 2022). Specifically, pro-inflammatory, M1-like macrophages are known to be the primary source of T cell-attracting chemokines, while anti-inflammatory, M2-like macrophages restrict T cell infiltration into the tumor (Italiani & Boraschi, 2014; Joyce & Fearon, 2015). Previously, a specific M2-like macrophage signature has been generated for five cancer types including AML and therefore, we investigated the abundance of M2-like macrophages in our pediatric AML cohort (Jiang et al., 2018). Interestingly, the estimated abundance of M2-like macrophages was inversely correlated with both the total T cell and cytotoxic T cell frequency in the BM (Spearman's r = -0.76 [95% CI: -0.89 to -0.51], P < 0.001, r = -0.64 [95% CI: -0.83 to -0.30], P = 0.001, respectively; **Fig. 2C** and **Extended Data Fig. 1F**). In line with this, we identified a significantly decreased M2-like macrophage abundance in immune-infiltrated samples compared to immune-depleted samples (two-sided P < 0.001; **Fig. 2D**). Notably, immune-depleted samples had significantly higher expression of the gene encoding arginase type II (*ARG2*), which is known to be crucial for AML blast-mediated polarization of monocytes into an M2-like phenotype (Mussai et al., 2013). Next, because it is unknown whether the abundance of M2-like macrophages affects the response to T cell-engaging immunotherapies in AML, we investigated whether the M2-like macrophage abundance is associated with poor response upon these therapies. However, pre-treatment gene expression data from immunotherapy-treated pediatric AML patients were not available and therefore, we used an immune-related gene expression profiling dataset of pre-treatment BM samples from 30 refractory or relapsed adult AML patients that were treated with flotetuzumab, a bispecific CD3 x CD123 antibody, in the context of a clinical trial (CP-MGD006-01; NCT02152956; obtained from Vadakekolathu et al., 2020). Interestingly, the M2-like macrophage abundance was significantly lower in patients with anti-leukemic activity (n=12) in comparison to non-responders (n=18; two-sided P < 0.001; **Fig. 2E**). In fact, the M2-like macrophage abundance outperformed several other known predictors of response to immunotherapy (area under the receiver operating

characteristic-curve: 0.852 [95% CI 0.71-0.99], *P* = 0.0012; **Fig. 2F**; Jiang et al., 2018, Ayers et al., 2017). In summary, we identified a relatively low abundance of M2-like macrophages in immune-infiltrated samples. In addition, we found that the M2-like macrophage abundance in the BM could be used as a potential biomarker for response to T cell-engaging immunotherapies in AML.

T cells cluster into spatially organized networks in the bone marrow of pediatric AML

Intriguingly, IHC performed to quantify the T cell infiltration in the BM revealed large networks of T cells in immune-infiltrated samples. Previously, it has been shown in mice that circulating naïve T cells home to the BM upon intravenous antigen administration, where they form dense networks of T cells and subsequently, are activated and differentiated towards effector and memory cells (Feuerer et al., 2003). Therefore, we investigated the spatial organization of T cells in pediatric immune-infiltrated, immune-depleted, and non-leukemic BM samples. T cell networks were defined as at least 10 directly interacting T cells (≤10 µm between adjacent nuclei), to minimize the chance of classifying randomly dispersed T cells as networks (Gaglia et al., 2022; **Fig. 3A**). Interestingly, T cell networks were detected in both AML groups and in controls, although significantly more frequent in immune-infiltrated samples compared to immune-depleted samples (*P* < 0.001; **Fig. 3B** and **Extended Data Table 2**). In fact, there was a strong correlation between the level of T cell infiltration and the number of T cell networks, albeit two out of eight immune-infiltrated patients had a relatively low number of networks (n=53; *r* = 0.86 [95% CI: 0.77-0.92], *P* < 0.001; **Fig. 3C**). Also, immune-infiltrated samples showed a trend towards having larger networks versus immune-depleted samples (*P*=0.086; **Fig. 3D**). Remarkably, we noticed that in the BM of immune-infiltrated samples with a multitude of large networks (>100 T cells), T cell network areas were largely devoid of AML cells, which could indicate local clearance of AML cells (determined using AML immunophenotypic markers; Pospori et al., 2020; **Fig. 3E-F**). In contrast, we did not identify such large T cell networks in the BM of immune-depleted samples (**Fig. 3G-H**). Taken together, these data show that spatially organized networks of T cells are widely abundant in pediatric AML patients with an immune-infiltrated BM, potentially reflecting local priming of anti-tumor immunity and/or immune-mediated elimination of AML cells.

Spatial transcriptomics reveals localized cellular and humoral immunity in *KMT2A*-rearranged patients

Subsequently, we wondered whether these large T cell networks in the BM resemble secondary lymphoid organ-like structures, as seen in solid cancers ('tertiary lymphoid structures', TLSs; Schumacher & Thommen, 2022). First, we checked whether T cells colocalized with $CD20^+$ B cells, since both T and B cells are the main components of secondary lymphoid organs (Ruddle & Akirav, 2009). Indeed, in four immune-infiltrated pediatric AML BM

samples, we detected large aggregates composed of T- and B cells ('lymphoid aggregates'; defined as networks of at least 100 directly interacting T cells that colocalized with a dense core of $CD20^+$ B cells). Interestingly, all four patients had *KMT2A*-rearranged AML. Importantly, these lymphoid aggregates were not classified as malignant upon pathological examination (Maccio et al., 2022). In fact, these aggregates had a non-trabecular localization, did not contain cells with atypical morphology, and showed a predominance of $CD3^+$ T cells, all features that have been associated with benign BM lymphoid aggregates (Maccio et al., 2022). In immune-depleted and non-leukemic control samples, we did not detect such lymphoid aggregates. Moreover, in solid cancers, TLSs arise in the context of chronic inflammation (Schumacher & Thommen, 2022), which may also have driven the formation of lymphoid aggregates in the BM of immune-infiltrated samples. To test whether lymphoid aggregates in the BM of pediatric AML patients represent structures similar to TLSs, we performed spatial transcriptomics using the GeoMx platform on bone biopsy tissue of two *KMT2A*-rearranged patients that had an immune-infiltrated BM with lymphoid aggregates (Merritt et al., 2020; **Fig. 4A-B**). As a control, we used tissue of one *KMT2A*-rearranged patient with an immune-infiltrated BM but without these aggregates (**Fig. 4C**). In total, we successfully sequenced 94 regions: (1) regions that contained lymphoid aggregates (n=20), (2) regions with T cell networks (n=26), and (3) regions that consisted of a mixture of AML-, T-, and B cells ('mixed' regions; n=48). Then, we explored which regions expressed TLS-associated genes using a previously generated TLS-signature (Meylan et al., 2022; **Fig. 4A-C**). In general, we observed concordant enrichment of the TLS-signature in areas we designated as regions containing lymphoid aggregates and hence, termed these structures 'TLS-like aggregates' (**Fig. 4A-B**). Surprisingly, one region in the biopsy without lymphoid aggregates was heavily enriched for the TLS-signature, possibly reflecting a forming or disintegrating TLS-like aggregate (**Fig. 4C**).

We next used *SpatialDecon*, a deconvolution approach optimized for spatial transcriptomic data, to examine the abundance of multiple immune and stromal cell types in these TLS-like aggregates (Danaher et al., 2022). To this end, we used safeTME, a scRNA-seq and flow-sorted bulk RNA-seq based reference profile of microenvironmental cell populations (Danaher et al., 2022). Importantly, the similarity in cellular composition identified using unsupervised hierarchical clustering (Euclidian distance; complete linkage) was highly concordant with our IHC-based distinction between regions (**Fig. 5A**). Interestingly, TLS-like aggregate regions and T cell networks both showed a significantly higher abundance of memory cytotoxic T cells, potentially because of local cytotoxic T cell priming (Philip & Schietinger, 2022; **Fig. 5B**). However, both types of regions also had a significantly higher abundance of Tregs, which may be a limiting factor of anti-tumor immunity (Joshi et al., 2015;

Fig. 5C). Because of this colocalization of cytotoxic T cells with Tregs, we interrogated the functional state of cytotoxic T cells using an additional scRNAseq reference profile specific for activated and resting BM T cells (Danaher et al., 2022). TLS-like aggregate regions not only had a significantly higher abundance of both activated and resting cytotoxic T cells, but also showed the highest ratio of activated to resting cytotoxic T cells in comparison to T cell network- and mixed regions (mean ratio of 0.72, 0.68, and 0.55, respectively), suggesting that cytotoxic T cells in TLS-like aggregates are present in an activated state despite the presence of Tregs (**Fig. 5D-E** & **Extended Data Fig. 2B**). Furthermore, the relatively high number of activated T cells may explain the absence of AML cells in these areas. In contrast to the T cell compartment, TLS-like aggregate regions had a significantly higher abundance of all measured B cell populations in comparison to mixed- and T cell network regions (**Fig. 5F-H**). Notably, differential gene expression analysis between TLS-like aggregate and mixed regions showed upregulation of genes indicative of immunoglobulin class-switching (*IGHG3*, *IGHG4*, *IGHA1*; **Extended Data Fig. 2A**). Also, we confirmed the enrichment of plasma and/or memory B cells in TLS-like aggregate regions using IHC, together suggesting anti-tumor antibody production in TLS-like aggregate regions (**Fig. 5I**; Akkaya et al., 2020). Other critical components of the TLSs seen in solid cancers are dendritic cells because of their pivotal role in priming of the immune response (Schumacher & Thommen, 2022). Interestingly, myeloid but not plasmacytoid dendritic cells were significantly enriched in TLS-like aggregate regions in comparison to mixed regions (**Fig. 5I** & **Extended Data Fig. 2C**). Furthermore, macrophages were significantly enriched in TLS-like aggregate and T cell network regions in comparison to mixed regions, which we validated using IHC (**Fig. 5J&M**). Specifically, TLS-like aggregates and T cell network regions showed a modest decrease in the abundance of M2-like macrophages compared to mixed regions, suggesting that the M1-like macrophage abundance was increased in TLS-like aggregate and T cell network regions (**Fig. 5K)**. In contrast, neutrophils had a significantly higher abundance in mixed regions (**Extended Data Fig. 2D**). Collectively, these results suggest that *KMT2A*-rearranged pediatric AML patients with an immune-infiltrated BM may harbor spatially organized areas of cellular and humoral anti-tumor immunity in the BM, which may translate to a positive effect on response upon T cell-engaging immunotherapies (Schumacher & Thommen, 2022).

Discussion

Pediatric cancers are characterized by a relatively low mutational burden and therefore, children are thought to be poor candidates for T cell-engaging immunotherapies (Majzner et al., 2017; Pfister et al., 2022). This prompted us to perform a multidimensional characterization of the tumor immune microenvironment in newly diagnosed children with *de novo* AML and non-leukemic controls. We identified a subset of patients with remarkably high T cell infiltration

in the BM, dissected the spatial organization of the immune compartment, and for the first time, unraveled the composition of TLS-like aggregates in the BM of AML.

Despite the relatively low mutational burden and the associated poor immunogenicity of pediatric cancers, previous work has shown that considerable variation in immune cell infiltration exists in cancers that are considered to be immunologically 'cold' (Gröbner et al., 2018; Dufva et al., 2020). Indeed, we observed wide variation in T cell infiltration in the BM of pediatric AML patients, including a subset that had remarkably high levels of T cell infiltration. These immune-infiltrated samples showed gene expression suggestive of an enrichment of GZMK^{+} cytotoxic T cells, which has been associated with response to immune checkpoint blockade in adult AML patients (Abbas et al., 2021). Hence, pediatric AML patients with an immune-infiltrated BM may show increased responses to immune checkpoint inhibitors in comparison to patients with an immune-depleted BM. Specifically, the immune checkpoint receptor genes *TIGIT* and *LAG3* were the most upregulated immune checkpoint genes in immune-infiltrated patients, suggesting that these less conventional checkpoint receptors may prove interesting immunotherapeutic targets in pediatric AML (Bailur et al., 2020; Lasry et al., 2022; Penter et al., 2023). Furthermore, we identified that immune-infiltrated samples harbored a significantly lower abundance of the immunosuppressive M2-like macrophages in comparison to immune-depleted samples. Therefore, repolarizing M2-like macrophages towards an M1-like phenotype could be a suitable immunotherapeutic option in pediatric AML patients with an immune-depleted BM (Duan & Luo, 2021; Li et al., 2022). Of interest, a recent study indicated that M2-like macrophages in the BM of adult AML patients showed increased expression of the immune checkpoints TIGIT and LAG-3 compared to healthy donors, and that TIGIT blockade was able to repolarize these M2-like macrophages to an M1-like phenotype (Brauneck et al., 2022). Thus, TIGIT and LAG-3 blockade may have beneficial effects on both the T cell and macrophage compartment, which encourages further evaluation of these agents in the preclinical setting.

In solid cancers, the importance of the spatial component of the immune response is widely recognized. For instance, in the so-called 'excluded' tumors, an immune response is triggered but not able to invade the tumor bed and hence, associates with poor response to immunotherapy (Bruni, Angell & Galon, 2020). In hematological malignancies, the spatial organization of the immune response is understudied, while potentially critical to the success of immunotherapeutic interventions. In our study, we identified large aggregates of T- and B cells in the leukemic BM that resembled gene expression characteristics of TLSs (Meylan et al., 2022). Importantly, pathology examination indicated that the TLS-like aggregates detected in immune-infiltrated pediatric AML samples in our cohort were not of malignant origin. In fact, these aggregates likely arose because of the chronically inflamed tumor microenvironment,

as seen with TLSs in solid cancers (Schumacher & Thommen, 2022). In line with this, we did not detect TLS-like aggregates in the immune-depleted or non-leukemic control samples. Furthermore, we dissected the composition of these TLS-like aggregates in the BM of pediatric AML patients, which turned out to be local hotspots of activated cytotoxic T cells, memory B cells, and plasma cells. Moreover, these hotspots were largely devoid of AML cells despite full-blown leukemia in other areas of the BM. Hence, these data suggest the presence of localized anti-tumor immunity in the BM of AML, which may have profound implications for future immunotherapy approaches. For instance, the increased abundance of plasma cells and the expression of class-switched immunoglobulin genes suggest the production of anti-tumor antibodies, which may lead to novel targets for antibody-based therapies through identification of the respective target antigens (Fridman et al., 2022). Likewise, the presence of TLS-like aggregates in AML may pave the way for new adoptive cell therapies with tumor-infiltrating T cells, since the T cells primed in these structures are likely to be tumor-reactive (Schumacher & Thommen, 2022). Current immunotherapies may also release the breaks of TLS-like aggregate-associated anti-tumor immunity, as illustrated by the results of a recent clinical trial in advanced soft-tissue sarcoma which showed that patients enrolled based on the presence of TLSs had an overall response rate of 30% to PD-1 blockade, opposed to 2.4% in an unselected cohort (Italiano et al., 2022).

Remarkably, all four patients with TLS-like aggregates in the BM had a *KMT2A*-rearrangement. Although we detected wide variation in T cell infiltration in patients with this cytogenetic alteration, the detection of these aggregates in patients with *KMT2A*-rearranged AML indicates that at least some of these patients, which have relatively poor outcomes upon chemotherapy, may be good candidates for immunotherapy (Van Weelderen et al., 2020). In conclusion, our results suggest the presence of distinct immune phenotypes in the BM of patients with pediatric AML including the presence of TLS-like aggregates in *KMT2A*-rearranged AML, suggesting that a subset of children with AML may benefit from T cell-engaging immunotherapies, and which encourages further study of these lymphoid structures in the BM in the context of immunotherapy in AML.

Online methods

Ethical regulation

This study complies with all relevant ethical regulations and was approved by the Institutional Review Board of the Princess Máxima Center for Pediatric Oncology (PMCLAB2021.207 & PMCLAB2021.238) and the Scientific Committee of the Dutch Nationwide Pathology Databank (PALGA: lzv2021-82; Casparie et al., 2007). All patients treated at the Princess Máxima Center provided written consent for banking and research use of these specimens,

according to the Declaration of Helsinki. Bone biopsy tissues acquired from external biobanks (n=28) were leftover material from standard care procedures and therefore, no informed consent was acquired, according to Dutch legislation and the code of conduct of the Committee on Regulation of Health Research (COREON).

Human patient samples

FFPE bone biopsies taken from the crista of children with treatment-naïve *de novo* AML were obtained from the Princess Máxima Center Biobank (n=15) and biobanks of 10 other Dutch hospitals (n=28), mediated by the Dutch National Tissue Portal. As controls, FFPE bone biopsies of age- and sex-matched children with treatment-naïve early-stage rhabdomyosarcoma were obtained from the Princess Máxima Center Biobank (n=10; non-leukemic controls). An experienced hemato-onco pathologist confirmed that these control biopsies resembled normal hematopoiesis and that there was no malignancy infiltrating the BM.

Immunohistochemistry staining and digital image analysis

Bone biopsies were cut into consecutive 4 µm sections and stained with hematoxylin and eosin (H&E). Conventional IHC was performed for CD3, CD3-CD4 (duplex), CD8, CD20, CD34, CD117, CD15, and IgM-IgG (duplex) using a Ventana Benchmark Ultra (Roche, Basel, Switzerland) automated staining instrument according to manufacturers' recommendations. A list of antibodies and suppliers is available in **Extended Data Table 3**. Digital scans of stained slides were obtained using a NanoZoomer scanner (Hamamatsu, Shizuoka, Japan). On 4 µm sections from three *KMT2A*-rearranged pediatric AML patients with an immune-infiltrated BM, we applied the FixVUE APC™ Kit (Ultivue Inc. Cambridge, MA, USA; CD20, CD68/CD163 cocktail, CD11c, and MHC-II) using the antibody conjugated DNA-barcoded multiplexed immunofluorescence method, as previously described (Manesse et al., 2020). The staining was performed on the BOND RX (Leica Biosystems, Wetzlar, Germany). To acquire an H&E staining on the same slide, the fluorescently labelled slides were soaked in PBS until the coverslips could be removed, and a standard H&E stain was performed using an Epredia Gemini (Epredia, Portsmouth, UK). Digital immunofluorescence and brightfield images were scanned on a Zeiss Axioscan Z1 (ZEISS, Oberkochen, Germany) and stacked with Ultivue's UltiStacker software. Whole-slide digital image analysis was performed in QuPath (V.0.3.2, Bankhead et al., 2017). Inside QuPath, the deep learning-based cell segmentation tool StarDist and the machine learning-based Random Trees classifier were used to quantify the number of positive cells per mm^2 (Schmidt et al., 2018). T cell networks were defined as at least 10 directly interacting $CD3^+$ T cells (≤ 10 µm between adjacent nuclei), detected using Delaunay Triangulation, and normalized per 10 cm^2 (Delaunay, 1934; Gaglia et al., 2022).

Large T cell networks of at least 100 directly interacting T cells that colocalized with a dense core of $CD20^+$ B cells were classified as lymphoid aggregates.

Immune-related gene expression profiling

Four consecutive sections of 10 µm from 5 immune-infiltrated and 18 immune-depleted FFPE bone biopsies (the non-leukemic controls' median value of cytotoxic T cells was used as the cut-off value) from a cytogenetically representative cohort of pediatric AML patients were used to isolate RNA and to perform immune-related gene expression profiling with the 770-gene PanCancer IO 360 panel, as previously described (Danaher et al., 2017; Vadakekolathu et al., 2020; NanoString, Seattle, WA, USA). After passing quality control, raw data were normalized using ROSALIND® according to Nanostring's recommendations (https://rosalind.bio/; San Diego, CA, USA). Normalized data were uploaded to the online iDEP platform and differentially expressed genes between immune-infiltrated and immune-depleted samples were identified using *DEseq2* with a false-discovery rate (FDR) cut-off of 0.05 and a minimum fold change of 2 (integrative Differential Expression and Pathway analysis; http://bioinformatics.sdstate.edu/idep96/; V.0.96; Ge, Son & Yao, 2018). Pathway analysis was performed using parametric gene set enrichment analysis with the GO Biological Processes gene set with an FDR of 0.05 (Ashburner et al., 2000; The Gene Ontology Consortium, 2020). The abundance of M2-like macrophages was estimated using a published gene signature of M2-like macrophages compared to M1-like macrophages, inside the TIDE environment (tide.dfci.harvard.edu/; Beyer et al., 2020; Jiang et al., 2018). Similarly, the T cell inflamed gene expression profile, the CD8-, IFN-*γ*-, and TIDE scores were all calculated using TIDE.

GeoMx Digital Spatial Profiling

5 µm thick FFPE bone biopsy sections from three *KMT2A*-rearranged pediatric AML patients with an immune-infiltrated BM were placed on the same slide and prepared for GeoMx Digital Spatial Profiling (DSP; NanoString), as previously described (Merritt et al., 2020). Slides were simultaneously incubated with immunofluorescent antibodies and GeoMx Whole Transcriptome Atlas profiling reagents. SYTO13 (S7575, Thermo Fisher,) was used for identification of nuclei, CD45 (NBP2-34528, Novus) for leukocytes, and CD3 (NBP2-54392AF647, Novus) for T cells. Stained slides were loaded onto the GeoMx instrument and scanned. Regions of interest (ROIs) were selected using the above-mentioned antibodies in combination with overlayed images of CD20, CD34, CD3-CD4 (duplex), and CD117 (IHC). Then, UV-photocleaved oligonucleotides were collected in separate wells and sequenced on the Nextseq2000 (Illumina, San Diego, CA, USA). In total, we successfully sequenced 94 regions (one failed quality control) with on average 273 cells per region (range: 156 to 778

cells). Raw data were normalized using Quartile 3 count (Q3) normalization in R (V.4.2.1) as per NanoString's recommendations (code is available in the vignette of the *Geomxtools* package). The expression of the TLS-signature as described by Meylan et al. was plotted in R on the scanned image using *SpatialOmicsOverlay* (Meylan et al., 2022). Spatial Deconvolution was performed in the GeoMx DSP Analysis Suite using both the safeTME and healthy adult BM T cell reference profiles (*SpatialDecon* package; cell reference profiles are available via https://github.com/Nanostring-Biostats/CellProfileLibrary; Danaher et al., 2022). Differential gene expression analysis between regions was performed using a linear mixed-effects model including random slope to correct for the fact that multiple regions come from the same biopsy, and the FDR method (code: *Geomxtools* package; minimum fold change of 2).

External pediatric and adult AML datasets

Single-cell RNA-sequencing (scRNAseq) data from 8 newly diagnosed pediatric AML patients were re-analyzed for cell-type specific *PDCD1*, *CTLA4*, *TIGIT*, and *LAG3* expression using the Tumor Immune Single-cell Hub (Bailur et al., 2020; Sun et al., 2021). Immune-related gene expression data (PanCancer IO 360 panel) from pre-treatment BM samples from 30 relapsed or refractory adult AML patients that were treated with flotetuzumab in the context of the CP-MGD006-01 clinical trial (NCT02152956) were kindly provided by Professor Sergio Rutella (Nottingham Trent University, England) and dr. Patrick Kaminker (MacroGenics, Rockville, MD, USA) and analyzed as described above.

Statistical analyses

Statistical analyses were performed with GraphPad Prism V.9.3.0 (GraphPad Software, LA Jolla, CA, USA). Differences between two independent groups were compared using the Mann-Whitney test. The correlation between two variables was evaluated using Spearman's *r*. To measure the area under the receiver operating characteristic curve, we employed the Wilson-Brown method. In case of multiple comparisons and no Gaussian distribution of residuals, we employed the Kruskal-Wallis test followed by Dunn's test for multiple comparisons including a Bonferroni correction. Hence for the multiple testing, $P<0.01$ was considered statistically significant in these comparisons. For all the other comparisons, $P<0.05$ was considered statistically significant.

Data availability

Sequencing data can be accessed from the Gene Expression Omnibus (nCounter data: GSEXXX; GeoMx data: GSEXXX; both normalized counts) and from the European Genome-

phenome Archive (EGA) database (https://ega-archive.org/studies/EGAXXX; raw nCounter and GeoMx data).

Acknowledgements

We would like to thank the staff of the University Medical Center Utrecht Tissue Facility for their excellent immunohistochemistry service (Domenico Castigliego, Petra van der Weide, Petra van der Kraak, Karina Timmer, Sven van Kempen), and the team at Utrecht Sequencing Facility for performing the NanoString experiments (nCounter and GeoMx) and for providing assistance with data-analysis (dr. Ies Nijman, Robin Geene, Pim Kloosterman). We are grateful to Professor Sergio Rutella (Notthingham Trent University) and dr. Patrick Kaminker (MacroGenics) for providing us with immune-related gene expression data from immunotherapy-treated adult AML samples. Dr. Ivette Deckers and dr. Annette Gijsbers (PALGA) performed essential work for the acquisition of bone biopsies from other hospitals. From the Princess Máxima Center for Pediatric Oncology, prof. dr. Gertjan Kaspers and dr. Bianca Goemans aided with identifying potential patients, the biobank staff (Jantien Woudstra, Marion Koopmans, dr. Edwin Sonneveld) helped to identify patient material, and Arie Maat aided with the sectioning of bone biopsy sections. Also, we would like to thank dr. Caroline Lindemans, members from the Heidenreich group (dr. Katarzyna Szoltysek, dr. Farnaz Barneh, dr. Mauricio Ferrao-Blanco, Elizabeth Schweighart, Nina van der Wilt), the Van Heesch group (dr. Ana Pinheiro-Lopes), and the single-cell sequencing facility (dr. Lindy Visser) at the Princess Máxima Center for Pediatric Oncology for carefully reading the manuscript and/or fruitful discussions. This work has been funded in part by a KIKA (329) program grant to O.H. Figure 1A and 3A have been created using BioRender.com.

Author contributions

Conceptualization: J.B.K, I.W., M.A.V., S.N., M.B., C.M.Z., O.H. Methodology: J.B.K, I.W., M.A.V., M.F., S.N., M.B., C.M.Z., O.H. Data acquisition: J.B.K., M.A.V., H.G.-K., R.M. Data analysis and interpretation: J.B.K., I.W., A.P. Writing – Original Draft: J.B.K.; Writing – Reviewing & Editing: all authors; Supervision: S.N., M.B., C.M.Z., O.H.

References

Abbas HA, Hao D, Tomczak K, et al. Single cell T cell landscape and T cell receptor repertoire profiling of AML in context of PD-1 blockade therapy. *Nat Commun*. 2021;12(1):6071.

Akkaya M, Kwak K, Pierce SK. B cell memory: building two walls of protection against pathogens. *Nat Rev Immunol*. 2020;20(4):229-238.

Ashburner M, Ball CA, Blake JA, et al. Gene ontology: tool for the unification of biology. The Gene Ontology Consortium. *Nat Genet*. 2000;25(1):25-29.

Ayers M, Lunceford J, Nebozhyn M, et al. IFN-γ-related mRNA profile predicts clinical response to PD-1 blockade. *J Clin Invest*. 2017;127(8):2930-2940.

Bailur JK, McCachren SS, Pendleton K, et al. Risk-associated alterations in marrow T cells in pediatric leukemia. *JCI Insight*. 2020;5(16):e140179.

Bankhead P, Loughrey MB, Fernández JA, et al. QuPath: Open source software for digital pathology image analysis. *Sci Rep*. 2017;7(1):16878.

Beyer M, Mallmann MR, Xue J, et al. High-resolution transcriptome of human macrophages. *PLoS One*. 2012;7(9):e45466.

Brauneck F, Fischer B, Witt M, et al. TIGIT blockade repolarizes AML-associated TIGIT$^+$ M2 macrophages to an M1 phenotype and increases CD47-mediated phagocytosis. *J Immunother Cancer*. 2022;10(12):e004794.

Bruni D, Angell HK, Galon J. The immune contexture and Immunoscore in cancer prognosis and therapeutic efficacy. *Nat Rev Cancer*. 2020;20(11):662-680.

Casparie M, Tiebosch AT, Burger G, et al. Pathology databanking and biobanking in The Netherlands, a central role for PALGA, the nationwide histopathology and cytopathology data network and archive. *Cell Oncol*. 2007;29(1):19-24.

Danaher P, Warren S, Dennis L, et al. Gene expression markers of Tumor Infiltrating Leukocytes. *J Immunother Cancer*. 2017;5:18.

Danaher P, Kim Y, Nelson B, et al. Advances in mixed cell deconvolution enable quantification of cell types in spatial transcriptomic data. *Nat Commun*. 2022;13(1):385

Daver N, Alotaibi AS, Bücklein V, Subklewe M. T-cell-based immunotherapy of acute myeloid leukemia: current concepts and future developments. *Leukemia*. 2021;35(7):1843-1863.

Delaunay B. Sur la sphère vide. *Bull. Acad. Sci. URSS*. 1934:793–800.

de Rooij JD, Zwaan CM, van den Heuvel-Eibrink M. Pediatric AML: From Biology to Clinical Management. *J Clin Med*. 2015;4(1):127-149.

Duan Z, Luo Y. Targeting macrophages in cancer immunotherapy. *Signal Transduct Target Ther*. 2021;6(1):127.

Dufva O, Pölönen P, Brück O, et al. Immunogenomic Landscape of Hematological Malignancies. *Cancer Cell*. 2020;38(3):380-399.e13.

Feuerer M, Beckhove P, Garbi N, et al. Bone marrow as a priming site for T-cell responses to blood-borne antigen. *Nat Med*. 2003;9(9):1151-1157.

Fridman WH, Meylan M, Petitprez F, Sun CM, Italiano A, Sautès-Fridman C. B cells and tertiary lymphoid structures as determinants of tumour immune contexture and clinical outcome. *Nat Rev Clin Oncol*. 2022;19(7):441-457.

Gaglia G, Burger M, Ritch CC, et al. Lymphocyte networks are dynamic communities in the immunoregulatory landscape of lung adenocarcinoma. *bioRxiv*. 2022-08.

Ge SX, Son EW, Yao R. iDEP: an integrated web application for differential expression and pathway analysis of RNA-Seq data. *BMC Bioinformatics*. 2018;19(1):534.

Gene Ontology Consortium. The Gene Ontology resource: enriching a GOld mine. *Nucleic Acids Res*. 2021;49(D1):D325-D334.

Gröbner SN, Worst BC, Weischenfeldt J, et al. The landscape of genomic alterations across childhood cancers. *Nature*. 2018;555(7696):321-327.

Hoch T, Schulz D, Eling N, Gómez JM, Levesque MP, Bodenmiller B. Multiplexed imaging mass cytometry of the chemokine milieus in melanoma characterizes features of the response to immunotherapy. *Sci Immunol*. 2022;7(70):eabk1692.

House IG, Savas P, Lai J, et al. Macrophage-Derived CXCL9 and CXCL10 Are Required for Antitumor Immune Responses Following Immune Checkpoint Blockade. *Clin Cancer Res*. 2020;26(2):487-504.

Italiani P, Boraschi D. From Monocytes to M1/M2 Macrophages: Phenotypical vs. Functional Differentiation. *Front Immunol*. 2014;5:514.

Italiano A, Bessede A, Pulido M, et al. Pembrolizumab in soft-tissue sarcomas with tertiary lymphoid structures: a phase 2 PEMBROSARC trial cohort. *Nat Med*. 2022;28(6):1199-1206.

Jiang P, Gu S, Pan D, et al. Signatures of T cell dysfunction and exclusion predict cancer immunotherapy response. *Nat Med*. 2018;24(10):1550-1558.

Joshi NS, Akama-Garren EH, Lu Y, et al. Regulatory T Cells in Tumor-Associated Tertiary Lymphoid Structures Suppress Anti-tumor T Cell Responses. *Immunity*. 2015;43(3):579-590.

Joyce JA, Fearon DT. T cell exclusion, immune privilege, and the tumor microenvironment. *Science*. 2015;348(6230):74-80.

Koedijk JB, van der Werf I, Calkoen FG, et al. Paving the Way for Immunotherapy in Pediatric Acute Myeloid Leukemia: Current Knowledge and the Way Forward. *Cancers (Basel)*. 2021;13(17):4364.

Lasry A, Nadorp B, Fornerod M, et al. An inflammatory state remodels the immune microenvironment and improves risk stratification in acute myeloid leukemia. *Nat Cancer*. 2023;4(1):27-42.

Li W, Wang F, Guo R, Bian Z, Song Y. Targeting macrophages in hematological malignancies: recent advances and future directions. *J Hematol Oncol*. 2022;15(1):110.

Maccio U, Rets AV. Lymphoid aggregates in bone marrow: a diagnostic pitfall. *J Clin Pathol*. 2022;75(12):807-814.

Majzner RG, Heitzeneder S, Mackall CL. Harnessing the Immunotherapy Revolution for the Treatment of Childhood Cancers. *Cancer Cell*. 2017;31(4):476-485.

Manesse M, Patel KK, Bobrow M, Downing SR. The InSituPlex® Staining Method for Multiplexed Immunofluorescence Cell Phenotyping and Spatial Profiling of Tumor FFPE Samples. *Methods Mol Biol*. 2020;2055:585-592.

Merritt CR, Ong GT, Church SE, et al. Multiplex digital spatial profiling of proteins and RNA in fixed tissue. *Nat Biotechnol*. 2020;38(5):586-599.

Meylan M, Petitprez F, Becht E, et al. Tertiary lymphoid structures generate and propagate anti-tumor antibody-producing plasma cells in renal cell cancer. *Immunity*. S2022;55(3):527-541.e5.

Mussai F, De Santo C, Abu-Dayyeh I, et al. Acute myeloid leukemia creates an arginase-dependent immunosuppressive microenvironment. *Blood*. 2013;122(5):749-758.

Penter L, Liu Y, Wolff JO, et al. Mechanisms of response and resistance to combined decitabine and ipilimumab for advanced myeloid disease. *Blood*. 2023;blood.2022018246.

Pfister SM, Reyes-Múgica M, Chan JKC, et al. A Summary of the Inaugural WHO Classification of Pediatric Tumors: Transitioning from the Optical into the Molecular Era. *Cancer Discov*. 2022;12(2):331-355.

Philip M, Schietinger A. $CD8^+$ T cell differentiation and dysfunction in cancer. *Nat Rev Immunol*. 2022;22(4):209-223.

Ruddle NH, Akirav EM. Secondary lymphoid organs: responding to genetic and environmental cues in ontogeny and the immune response. *J Immunol*. 2009;183(4):2205-2212.

Schmidt U, Weigert M, Broaddus C et al. Cell detection with star-convex polygons. *International Conference on Medical Image Computing and Computer-Assisted Intervention*. 2018;265-273.

Schumacher TN, Thommen DS. Tertiary lymphoid structures in cancer. *Science*. 2022;375(6576):eabf9419.

Serroukh Y, Hébert J, Busque L, et al. Blasts in context: the impact of the immune environment on acute myeloid leukemia prognosis and treatment. *Blood Rev*. 2023;57:100991.

Sun D, Wang J, Han Y, et al. TISCH: a comprehensive web resource enabling interactive single-cell transcriptome visualization of tumor microenvironment. *Nucleic Acids Res*. 2021;49(D1):D1420-D1430.

Vadakekolathu J, Lai C, Reeder S, et al. TP53 abnormalities correlate with immune infiltration and associate with response to flotetuzumab immunotherapy in AML. *Blood Adv*. 2020;4(20):5011-5024.

Vadakekolathu J, Minden MD, Hood T, et al. Immune landscapes predict chemotherapy resistance and immunotherapy response in acute myeloid leukemia. *Sci Transl Med*. 2020;12(546):eaaz0463.

Van Weelderen RE, Klein K, Goemans BF et al. Outcomes of (novel) subgroups in 1257 pediatric patients with KMT2A-rearranged acute myeloid leukemia (AML) and the significance of minimal residual disease (MRD) status: A retrospective study by the I-BFM-SG. *Blood*. 2020;136:26-27.

Wellenstein MD, de Visser KE. Cancer-Cell-Intrinsic Mechanisms Shaping the Tumor Immune Landscape. *Immunity*. 2018;48(3):399-416.

Ye Q, Song DG, Poussin M, et al. CD137 accurately identifies and enriches for naturally occurring tumor-reactive T cells in tumor. *Clin Cancer Res*. 2014;20(1):44-55.

Figure Legends

Figure 1. Spatial analysis of the bone marrow immune microenvironment in pediatric AML and non-leukemic controls.

(A) Schematic overview of the study population, used techniques, and the digital image analysis pipeline. (B-C) Representative bone biopsy images acquired from a treatment-naïve pediatric AML patient (B) and non-leukemic control (C) showing H&E staining, $CD3^+$ T cells (CD3 in brown), and $CD8^+$ T cells (CD8 in brown). White lobules indicate adipocytes. (D-E) Comparison of the normalized abundance of $CD3^+$ T cells (D) and $CD8^+$ T cells (E) in the BM between pediatric AML patients and non-leukemic controls. (F-G) Normalized abundance of $CD3^+$ T cells (F) and $CD8^+$ T cells (G) per cytogenetic pediatric AML subgroup. 'Normal' indicates normal karyotype, while 'Others' is a merge of cytogenetic abnormalities different from the four defined cytogenetic subgroups.

Figure 2. Transcriptional differences between immune-infiltrated and immune-depleted pediatric AML samples.

(A) Volcano plot of differentially expressed genes between immune-infiltrated and immune-depleted pediatric AML BM samples, identified using *DEseq2* with an FDR cut-off of 0.05 and minimum fold change (FC) of 2. (B) Parametric gene set enrichment analysis of differentially expressed genes between immune-infiltrated (orange) and immune-depleted samples (blue) using the GO Biological Processes gene set with an FDR cut-off of 0.05. Values in front of the biological processes indicate *P* values. (C) Correlation plot of the inverse correlation between the M2-like macrophage abundance and the normalized number of $CD3^+$ T cells, calculated using Spearman correlation. (D-E) Comparison of the M2-like macrophage abundance between immune-infiltrated (n=5) and immune-depleted (n=18) BM samples (D) and between BM samples of refractory or relapsed (R/R) adult AML patients with anti-leukemic activity (ALA) or non-responders (NR) to treatment with the bispecific antibody flotetuzumab (E). (F) Area under the receiver operating characteristic curves measuring the predictive ability of the M2-like macrophage abundance (black), T cell inflamed gene expression profile (GEP; pink), CD8 score (blue), IFN-*γ* score (green), and the tumor immune dysfunction and exclusion score (TIDE; orange) in pre-treatment R/R adult AML samples for response to flotetuzumab.

Figure 3. Immune-infiltrated pediatric AML samples harbor an increased abundance of spatially organized T cell networks.

(A) Illustration of the identification of directly interacting T cells (above) and T cell networks (below) using Delaunay Triangulation. (B) Comparison of the normalized abundance of T cell

networks between immune-infiltrated, immune-depleted, and non-leukemic control samples. (C) Correlation plot of the positive correlation between the normalized number of $CD3^+$ T cells and the normalized number of T cell networks in both AML and non-leukemic control samples (n=53), calculated using Spearman correlation. (D) Comparison of the average number of T cells in a network between immune-infiltrated, immune-depleted, and non-leukemic control samples. (E-F) Representative images of an immune-infiltrated pediatric AML BM sample with multiple large T cell clusters (>100 T cells; CD3 in brown; E) that are largely devoid of AML cells (CD117 in brown, patient-specific AML immunophenotypic marker; F). (G-H). Representative images of an immune-depleted pediatric AML BM sample without T cell clusters (CD3 in brown; G) and widely dispersed AML cells (CD117 in brown; patient-specific AML immunophenotypic marker; H).

Figure 4. Spatial transcriptomics reveals gene expression characteristics of tertiary lymphoid structures in *KMT2A*-rearranged immune-infiltrated pediatric AML samples.

(A-C) Images of the bone biopsy sections that show the expression levels of a previously published TLS-signature in distinct regions of two lymphoid aggregate (LA)-positive (A+B) *KMT2A*-rearranged immune-infiltrated pediatric AML samples and one LA-negative (C) *KMT2A*-rearranged immune-infiltrated pediatric AML sample, next to immunohistochemistry-based images of $CD3^+$ T cells, $CD20^+$ B cells, and $CD117^+$ (A+C) or $CD4^+$ (B) AML cells. Orange arrows indicate LA-containing regions.

Figure 5. Spatial deconvolution identifies localized cellular and humoral immunity in *KMT2A*-rearranged immune-infiltrated pediatric AML samples.

(A) Dendrogram and bar plot of absolute immune- and stromal-cell abundance scores, calculated by applying the *SpatialDecon* algorithm to spatial transcriptomic data from three *KMT2A*-rearranged immune-infiltrated pediatric AML BM samples. Regions are divided in separate clusters based on similarity (unsupervised hierarchical clustering; Euclidian distance; complete linkage). The legend on the right indicates which type of cell is shown in the bar plot and for which type of region the cell composition is shown. (B-K) Comparisons of the abundance scores of several immune- and stromal cell types between mixed regions (n=48), T cell network regions (n=26), and TLS-like aggregate regions (n=20). Tregs indicates regulatory T cells, and DCs indicate dendritic cells. (I) Whole-slide bone biopsy image with a CD3 stain (brown) for T cells (above), and a magnified image illustrating the presence of IgM^+- (brown) and IgG^+-cells (purple) in the T cell rich area that is part of an TLS-like aggregate. (M) Magnifications of the T cell rich area shown in the whole-slide image shown in Figure I, showing the presence of $CD11c^+$ $CD68/CD163^+$ macrophages (red arrows) in the TLS-like aggregate region.

Extended Data Figure 1. Cell-type specific gene expression of immune checkpoint genes in pediatric AML.

(A) UMAP of cell populations identified in BM samples from 8 newly diagnosed pediatric AML patients using scRNAseq by Bailur et al. (B-E) Cell-type specific expression of *PDCD1* (B), *CTLA4* (C), *TIGIT* (D), *LAG3* (E) in the scRNAseq dataset. (F) Correlation plot of the inverse correlation between the M2-like macrophage abundance and the normalized number of $CD8^+$ T cells, calculated using Spearman correlation. CD8Tex: exhausted cytotoxic T cells; CD8Tem: effector memory cytotoxic T cells; cDC1: conventional dendritic cells type I; EryPro: erythroid progenitors; M1: M1-like macrophages.

Extended Data Figure 2. Region-specific gene expression and deconvoluted cell type abundance in the bone marrow of *KMT2A*-rearranged pediatric AML.

(A) Volcano plot of differentially expressed genes between TLS-like aggregate regions and mixed regions, identified using a linear mixed-effects model including random slope and the FDR method. FC indicates fold change. (B-D) Comparisons of the ratio between activated and resting cytotoxic T cells (B), the abundance scores of plasmacytoid dendritic cells (C), and neutrophils (D) between mixed regions (n=48), T cell network regions (n=26), and TLS-like aggregate regions (n=20).

Index of supplemental tables

Extended Data Table 1. Patient characteristics from 43 treatment-naïve pediatric patients with AML and 10 non-leukemic controls.

Extended Data Table 2. Number of T cell networks and TLS-like aggregates for each patient.

Extended Data Table 3. Antibodies used for immunohistochemistry of bone biopsy tissue.

Extended Data Table 1. Patient characteristics from 43 treatment-naïve pediatric patients with AML and 10 treatment-naïve non-leukemic controls.

ID	Sex	%BM Myelo-blasts	FAB	Cytogenetic alterations	Molecular aberrations	Immune infiltration	GEP + Spatial Tx
AML1	male	32	M2	NA	NA	Infiltrated	GEP
AML2	female	51	M5	KMT2Ar	none	Infiltrated	GEP + Spatial Tx
AML3	male	NA	NA	KMT2Ar	none	Infiltrated	GEP
AML4	male	55	NA	KMT2Ar	none	Infiltrated	GEP
AML5	male	28	NA	KMT2Ar, Trisomy-8	none	Infiltrated	Spatial Tx
AML6	male	44	NA	KMT2Ar	none	Infiltrated	GEP + Spatial Tx
AML7	male	39	NA	inv(16)	none	Infiltrated	
AML8	male	81	NA	t(8;21), 8q-deletion, Y-chromosome deletion	EXT1mut + RAD21mut	Infiltrated	
AML9	male	63	NA	KMT2Ar	none	Depleted	
AML10	male	81	NA	KMT2Ar	none	Depleted	
AML11	male	73	M5	inv(16)	none	Depleted	
AML12	male	77	M2	t(8;21)	none	Depleted	GEP
AML13	female	NA	NA	Normal karyotype	NPM1mut + WT-1mut	Depleted	GEP
AML14	male	50	M2	t(8;21)	none	Depleted	
AML15	female	14	M6	NA	NA	Depleted	
AML16	male	88	M1	t(8;21)	none	Depleted	GEP
AML17	female	31	M0	Normal karyotype	none	Depleted	
AML18	male	10	M7	NA	NA	Depleted	
AML19	male	NA	M5	NA	NA	Depleted	
AML20	female	NA	M6	NA	NA	Depleted	

AML21	female	72	M4	Monosomy-7	none	Depleted	GEP
AML22	male	94	M5	KMT2Ar	none	Depleted	GEP
AML23	male	98	M5	KMT2Ar	none	Depleted	GEP
AML24	female	20	NA	NA	NA	Depleted	GEP
AML25	male	8	M7	Trisomy-8	none	Depleted	GEP
AML26	male	80	M5	KMT2Ar	none	Depleted	GEP
AML27	male	36	M2	t(8;21)	WT-1mut	Depleted	GEP
AML28	female	69	NA	KMT2Ar	none	Depleted	GEP
AML29	male	45	M2	NA	NA	Depleted	GEP
AML30	male	39	M2	NA	NA	Depleted	GEP
AML31	female	NA	NA	NA	NA	Depleted	
AML32	female	38	NA	inv(16)	none	Depleted	GEP
AML33	female	34	NA	Normal karyotype	NPM1mut	Depleted	GEP
AML34	male	NA	NA	Normal karyotype	FLT3-ITDmut	Depleted	GEP
AML35	male	92	M5	KMT2Ar	none	Depleted	
AML36	female	90	M5	KMT2Ar	none	Depleted	
AML37	male	32	NA	9q-deletion	none	Depleted	
AML38	male	18	NA	Normal karyotype	none	Depleted	
AML39	male	0	NA	Normal karyotype	NPM1mut	Depleted	
AML40	male	12	NA	t(6;9)	WT1mut + NRASmut	Depleted	
AML41	female	5	NA	t(5;11)	none	Depleted	
AML42	male	63	NA	Monosomy-7, gain chromosome -13	TP53mut, RUNX1mut, SUZ12mut	Depleted	GEP
AML43	male	92	M5	KMT2Ar	NRASmut	Depleted	GEP
CTRL1	male	1	Not applicable				
CTRL2	female	0	Not applicable				
CTRL3	female	1	Not applicable				
CTRL4	male	2	Not applicable				
CTRL5	female	3	Not applicable				

CTRL6	male	1	Not applicable
CTRL7	male	1	Not applicable
CTRL8	male	0	Not applicable
CTRL9	male	2	Not applicable
CTRL10	female	1	Not applicable

AML: acute myeloid leukemia; BM: bone marrow; CTRL: non-leukemic control; dx: diagnosis; FAB: French-American-British (classification); GEP: gene expression profiling; KMT2Ar: KMT2A-rearranged; mut: mutation; NA: not available; Spatial Tx: spatial transcriptomics.

Extended Data Table 2. Number of T cell networks and TLS-like aggregates for each patient.

		T cell network number (by size)				
ID	**Immune infiltration**	**10-30 cells**	**31-99 cells**	**100-500 cells**	**>500 cells**	**TLS-like aggregates**
AML1	Infiltrated	161	30	11	1	NA
AML2	Infiltrated	191	57	15	8	6
AML3	Infiltrated	473	62	11	0	11
AML4	Infiltrated	92	11	1	0	1
AML5	Infiltrated	22	1	0	0	0
AML6	Infiltrated	320	48	7	1	4
AML7	Infiltrated	138	2	0	0	0
AML8	Infiltrated	18	0	0	0	0
AML9	Depleted	541	61	0	0	0
AML10	Depleted	242	9	0	0	0
AML11	Depleted	0	0	0	0	0
AML12	Depleted	0	0	0	0	0
AML13	Depleted	1	1	0	0	0
AML14	Depleted	0	0	0	0	0
AML15	Depleted	5	0	0	0	0
AML16	Depleted	3	0	0	0	0
AML17	Depleted	3	0	0	0	0
AML18	Depleted	1	0	0	0	0
AML19	Depleted	0	0	0	0	0
AML20	Depleted	3	0	0	0	0
AML21	Depleted	0	0	0	0	0
AML22	Depleted	6	0	0	0	0
AML23	Depleted	29	0	0	0	0
AML24	Depleted	82	4	1	0	NA
AML25	Depleted	4	0	0	0	0
AML26	Depleted	1	0	0	0	0
AML27	Depleted	1	0	0	0	0
AML28	Depleted	30	0	0	0	0
AML29	Depleted	8	1	0	0	0
AML30	Depleted	10	0	1	0	1
AML31	Depleted	6	0	0	0	0

AML32	Depleted	0	0	0	0	0
AML33	Depleted	0	0	0	0	0
AML34	Depleted	7	0	0	0	0
AML35	Depleted	27	1	0	0	0
AML36	Depleted	0	0	0	0	0
AML37	Depleted	2	1	0	0	0
AML38	Depleted	0	0	0	0	0
AML39	Depleted	19	1	0	0	0
AML40	Depleted	5	0	0	0	0
AML41	Depleted	51	7	0	0	0
AML42	Depleted	58	3	0	0	0
AML43	Depleted	74	7	1	0	NA
CTRL1	Control	11	0	0	0	0
CTRL2	Control	3	0	0	0	0
CTRL3	Control	8	0	0	0	0
CTRL4	Control	88	5	0	0	0
CTRL5	Control	62	5	0	0	0
CTRL6	Control	29	5	0	0	0
CTRL7	Control	63	0	0	0	0
CTRL8	Control	19	0	0	0	0
CTRL9	Control	46	1	0	0	0
CTRL10	Control	34	3	0	0	0

AML: acute myeloid leukemia; CTRL: non-leukemic control; TLS: tertiary lymphoid structure; NA: the presence of TLS-like aggregates could not be assessed in these biopsies since a $CD20^+$ B cell stain was lacking.

Extended Data Table 3. Antibodies used for immunohistochemistry of bone biopsy tissue.

Antibody	Code	Supplier	Catalog No.	Dilution
CD3	2GV6	Roche	05278422001	NA
CD4	SP35	Roche	05552737001	NA
CD8	SP57	Roche	5973248001	NA
CD20	L26	Roche	5267099001	NA
CD15	MMA	Roche	5266904001	NA
CD34	QBEnd/10	Roche	6389320001	NA
CD117	EP10	Roche	790-7061	NA
IgM	GA513	Dako	GA51361-2	1:24.000
IgG	GA512	Dako	GA51261-2	1:60.000

NA: Not applicable.

Figure 1

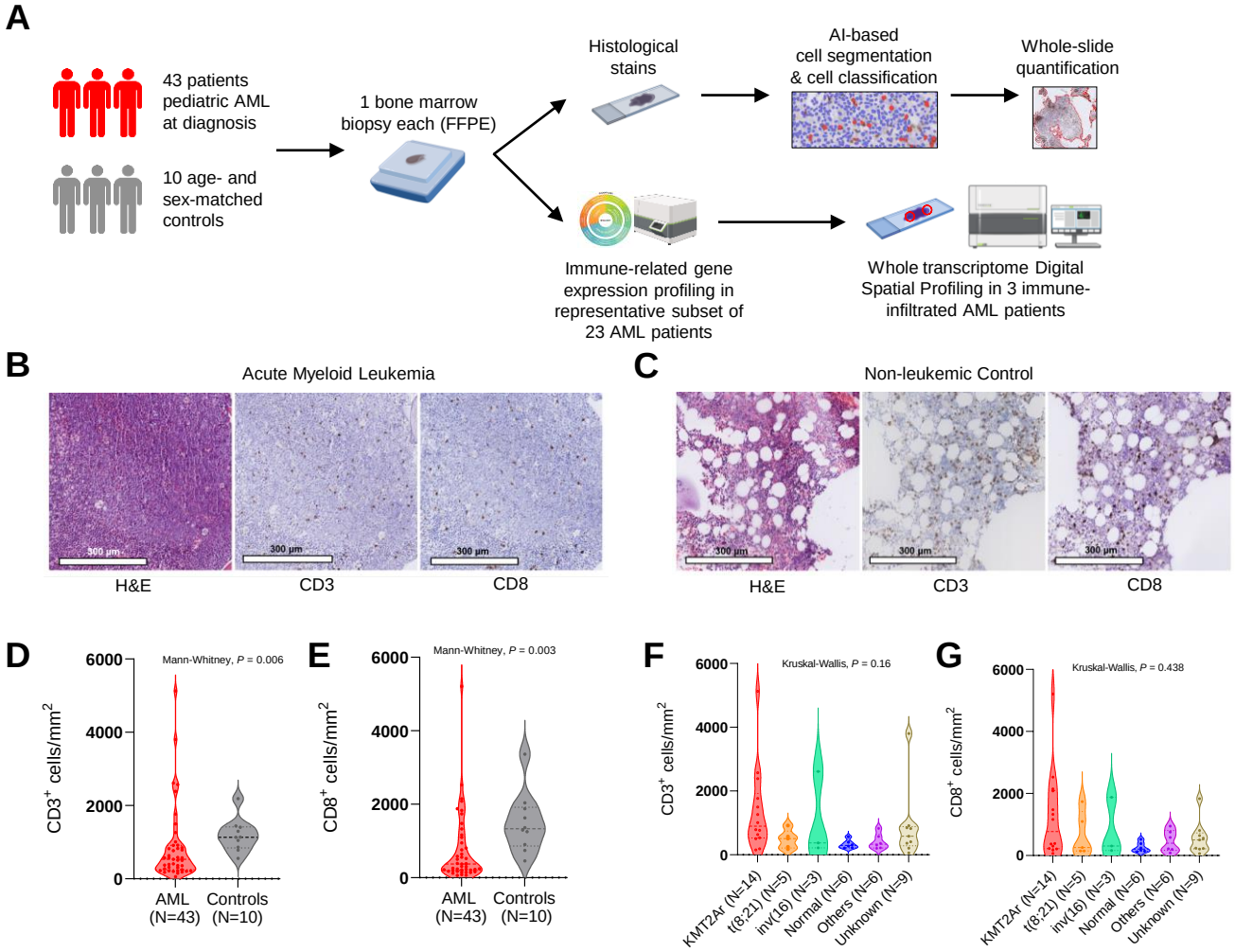
A
43 patients pediatric AML at diagnosis
10 age- and sex-matched controls
1 bone marrow biopsy each (FFPE)
Histological stains
AI-based cell segmentation & cell classification
Whole-slide quantification
Immune-related gene expression profiling in representative subset of 23 AML patients
Whole transcriptome Digital Spatial Profiling in 3 immune-infiltrated AML patients
B
Acute Myeloid Leukemia
H&E
CD3
CD8
C
Non-leukemic Control
H&E
CD3
CD8
300 µm
D
Mann-Whitney, P = 0.006
CD3+ cells/mm2
AML (N=43)
Controls (N=10)
E
Mann-Whitney, P = 0.003
CD8+ cells/mm2
AML (N=43)
Controls (N=10)
F
Kruskal-Wallis, P = 0.16
CD3+ cells/mm2
KMT2Ar (N=14)
t(8;21) (N=5)
inv(16) (N=3)
Normal (N=6)
Others (N=6)
Unknown (N=9)
G
Kruskal-Wallis, P = 0.438
CD8+ cells/mm2
KMT2Ar (N=14)
t(8;21) (N=5)
inv(16) (N=3)
Normal (N=6)
Others (N=6)
Unknown (N=9)

Figure 2

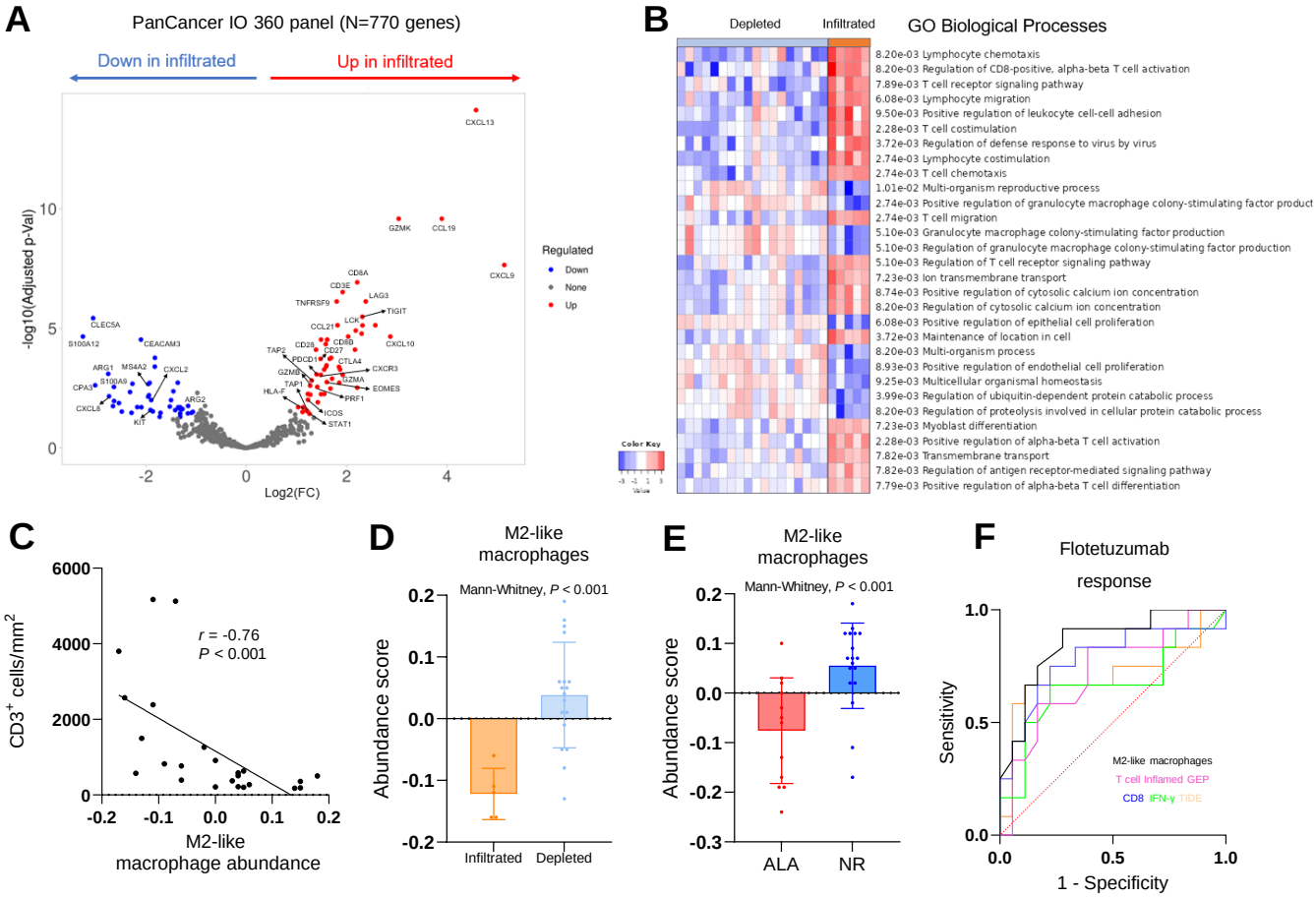
A
PanCancer IO 360 panel (N=770 genes)
Down in infiltrated
Up in infiltrated
-log10(Adjusted p-Val)
Log2(FC)
Regulated
Down
None
Up
B
Depleted
Infiltrated
GO Biological Processes
8.20e-03 Lymphocyte chemotaxis
8.20e-03 Regulation of CD8-positive, alpha-beta T cell activation
7.89e-03 T cell receptor signaling pathway
6.08e-03 Lymphocyte migration
9.50e-03 Positive regulation of leukocyte cell-cell adhesion
2.28e-03 T cell costimulation
3.72e-03 Regulation of defense response to virus by virus
2.74e-03 Lymphocyte costimulation
2.74e-03 T cell chemotaxis
1.01e-02 Multi-organism reproductive process
2.74e-03 Positive regulation of granulocyte macrophage colony-stimulating factor product
2.74e-03 T cell migration
5.10e-03 Granulocyte macrophage colony-stimulating factor production
5.10e-03 Regulation of granulocyte macrophage colony-stimulating factor production
5.10e-03 Regulation of T cell receptor signaling pathway
7.23e-03 Ion transmembrane transport
8.74e-03 Positive regulation of cytosolic calcium ion concentration
8.20e-03 Regulation of cytosolic calcium ion concentration
6.08e-03 Positive regulation of epithelial cell proliferation
3.72e-03 Maintenance of location in cell
8.20e-03 Multi-organism process
8.93e-03 Positive regulation of endothelial cell proliferation
9.25e-03 Multicellular organismal homeostasis
3.99e-03 Regulation of ubiquitin-dependent protein catabolic process
8.20e-03 Regulation of proteolysis involved in cellular protein catabolic process
7.23e-03 Myoblast differentiation
2.28e-03 Positive regulation of alpha-beta T cell activation
7.82e-03 Transmembrane transport
7.82e-03 Regulation of antigen receptor-mediated signaling pathway
7.79e-03 Positive regulation of alpha-beta T cell differentiation
Color Key
C
CD3+ cells/mm2
r = -0.76
P < 0.001
M2-like macrophage abundance
D
M2-like macrophages
Mann-Whitney, P < 0.001
Abundance score
Infiltrated
Depleted
E
M2-like macrophages
Mann-Whitney, P < 0.001
Abundance score
ALA
NR
F
Flotetuzumab response
Sensitivity
1 - Specificity
M2-like macrophages
T cell Inflamed GEP
CD8 IFN-γ TIDE

Figure 3

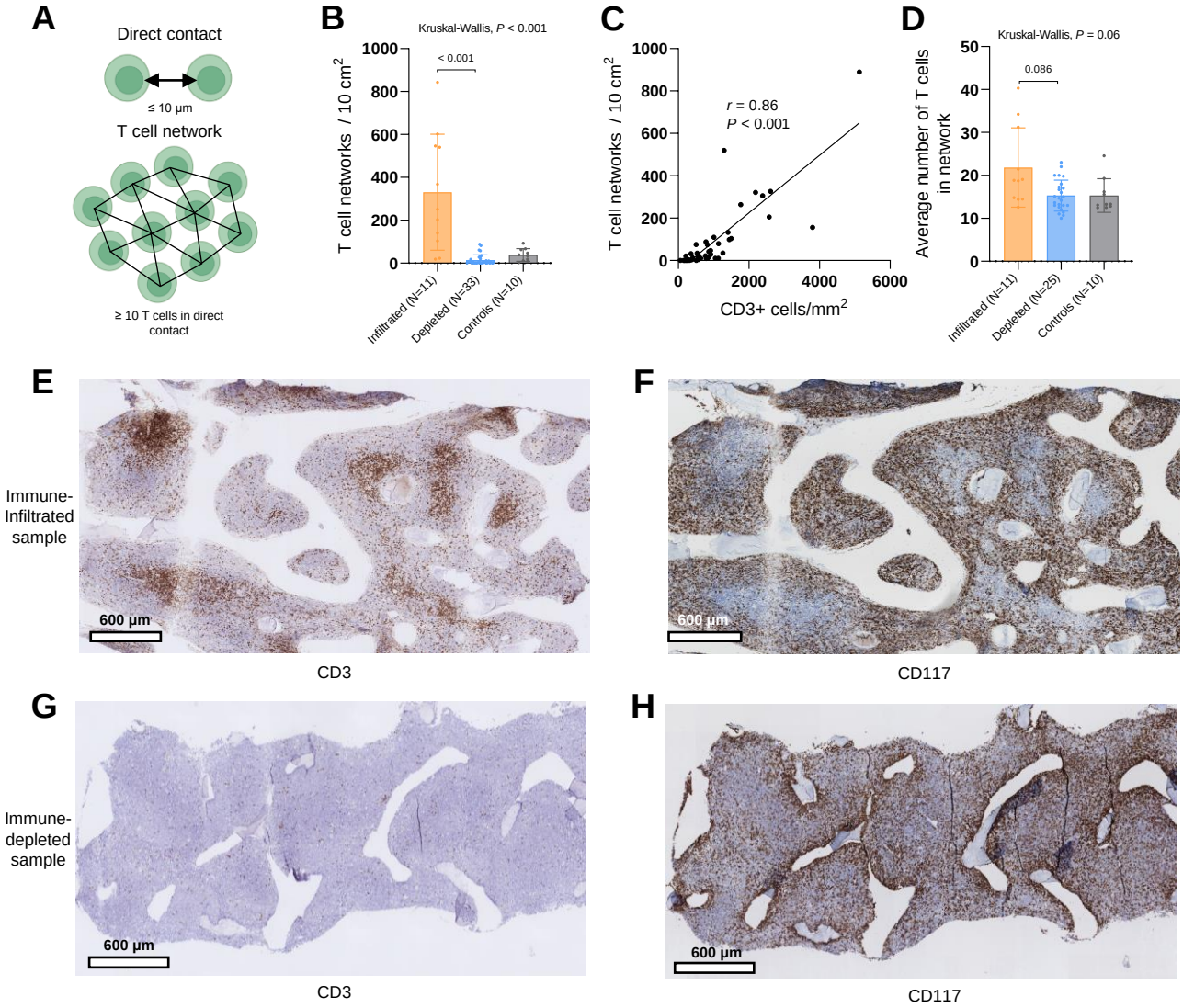
A
Direct contact
≤ 10 µm
T cell network
≥ 10 T cells in direct contact
B
Kruskal-Wallis, P < 0.001
< 0.001
T cell networks / 10 cm2
1000
800
600
400
200
0
Infiltrated (N=11)
Depleted (N=33)
Controls (N=10)
C
r = 0.86
P < 0.001
T cell networks / 10 cm2
CD3+ cells/mm2
0
2000
4000
6000
D
Kruskal-Wallis, P = 0.06
0.086
Average number of T cells in network
50
40
30
20
10
0
Infiltrated (N=11)
Depleted (N=25)
Controls (N=10)
E
Immune-Infiltrated sample
600 µm
CD3
F
600 µm
CD117
G
Immune-depleted sample
600 µm
CD3
H
600 µm
CD117

Figure 4

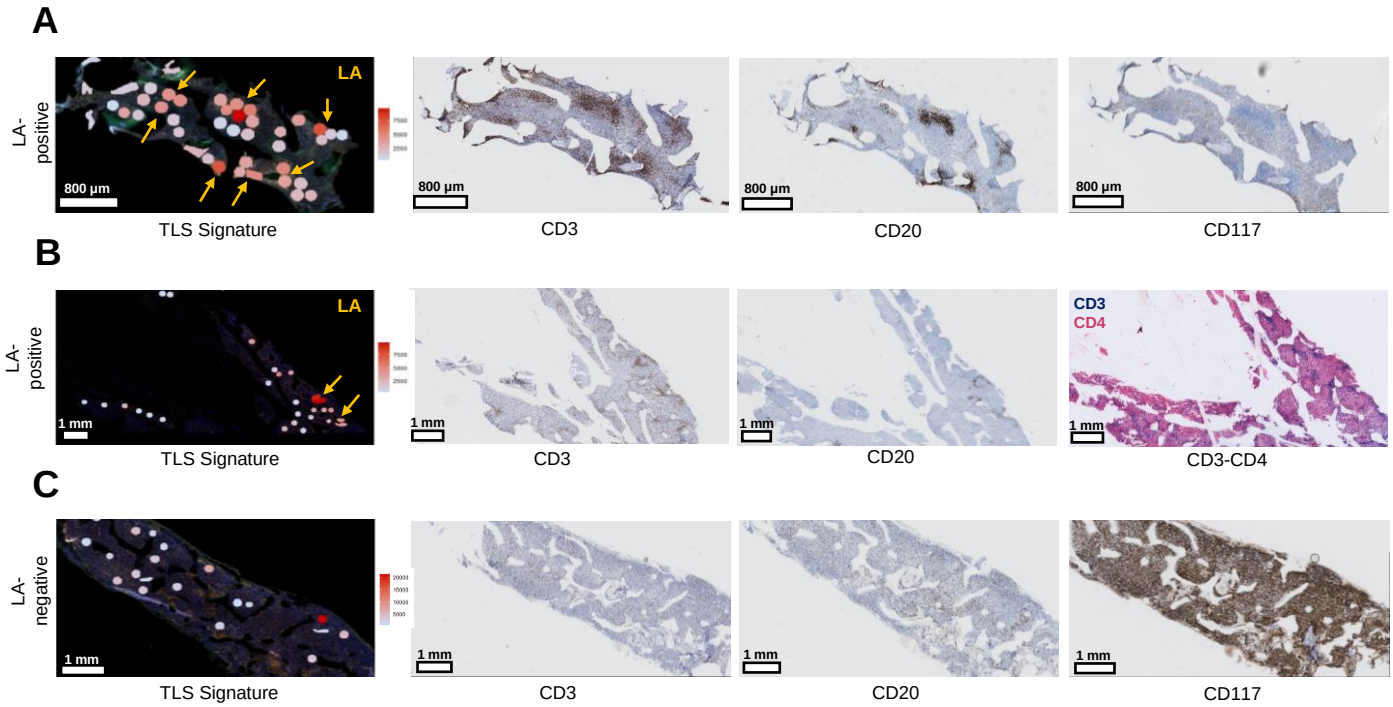
A
LA-positive
LA
800 µm
TLS Signature
CD3
CD20
CD117
B
LA-positive
LA
1 mm
TLS Signature
CD3
CD20
CD3
CD4
CD3-CD4
C
LA-negative
1 mm
TLS Signature
CD3
CD20
CD117

Figure 5

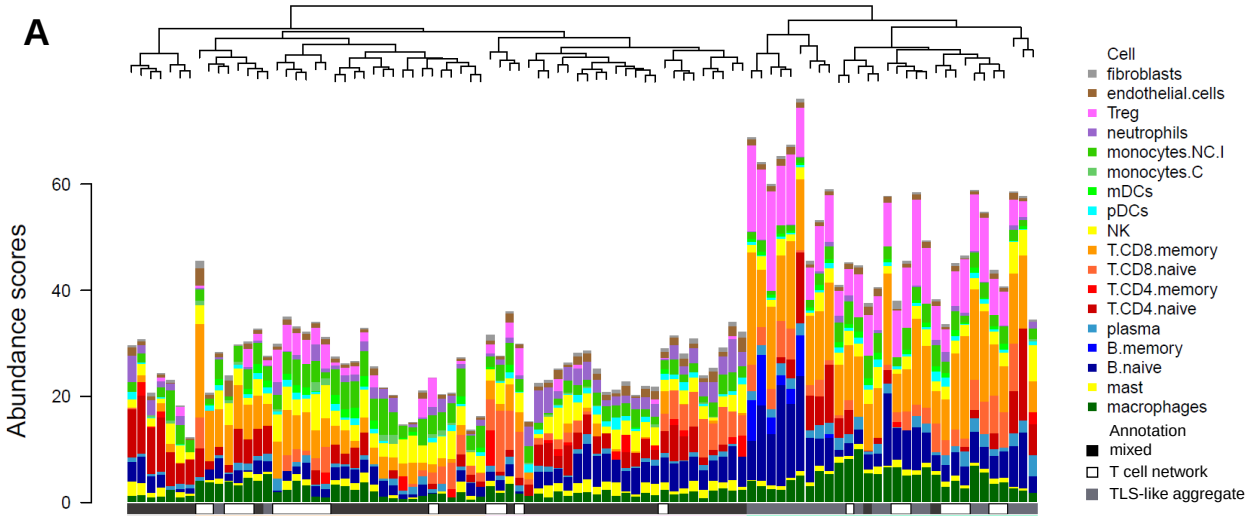
A
Abundance scores
60
40
20
0
Cell
fibroblasts
endothelial.cells
Treg
neutrophils
monocytes.NC.I
monocytes.C
mDCs
pDCs
NK
T.CD8.memory
T.CD8.naive
T.CD4.memory
T.CD4.naive
plasma
B.memory
B.naive
mast
macrophages
Annotation
mixed
T cell network
TLS-like aggregate

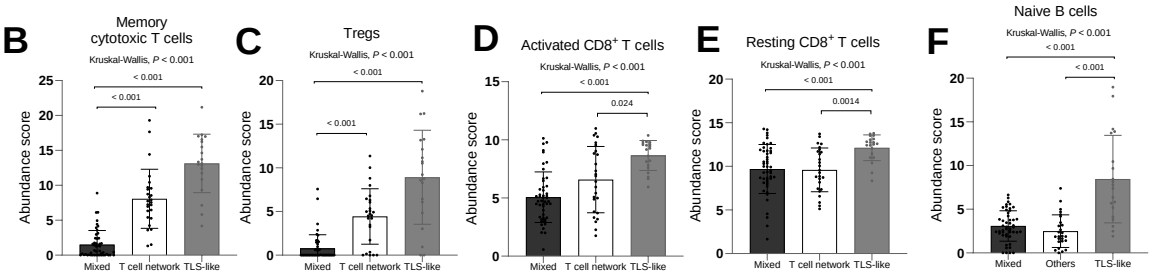
B
Memory cytotoxic T cells
Kruskal-Wallis, P < 0.001
< 0.001
< 0.001
Abundance score
Mixed
T cell network
TLS-like
C
Tregs
Kruskal-Wallis, P < 0.001
< 0.001
< 0.001
D
Activated CD8+ T cells
Kruskal-Wallis, P < 0.001
< 0.001
0.024
E
Resting CD8+ T cells
Kruskal-Wallis, P < 0.001
< 0.001
0.0014
F
Naive B cells
Kruskal-Wallis, P < 0.001
< 0.001
< 0.001
Mixed
Others
TLS-like

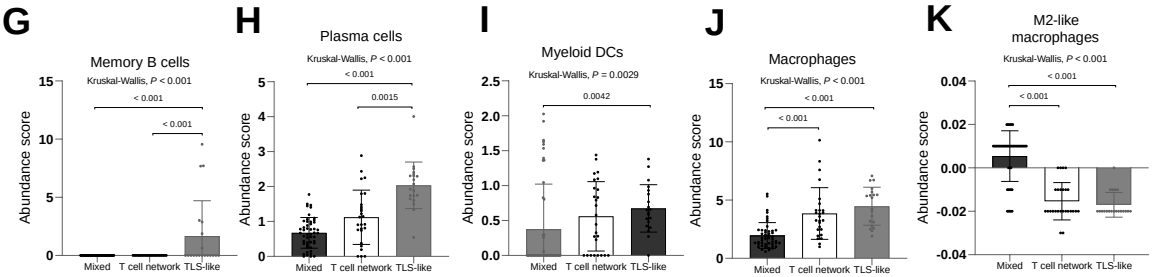
G
Memory B cells
Kruskal-Wallis, P < 0.001
< 0.001
< 0.001
H
Plasma cells
Kruskal-Wallis, P < 0.001
< 0.001
0.0015
I
Myeloid DCs
Kruskal-Wallis, P = 0.0029
0.0042
J
Macrophages
Kruskal-Wallis, P < 0.001
< 0.001
< 0.001
K
M2-like macrophages
Kruskal-Wallis, P < 0.001
< 0.001
< 0.001
Abundance score
Mixed
T cell network
TLS-like

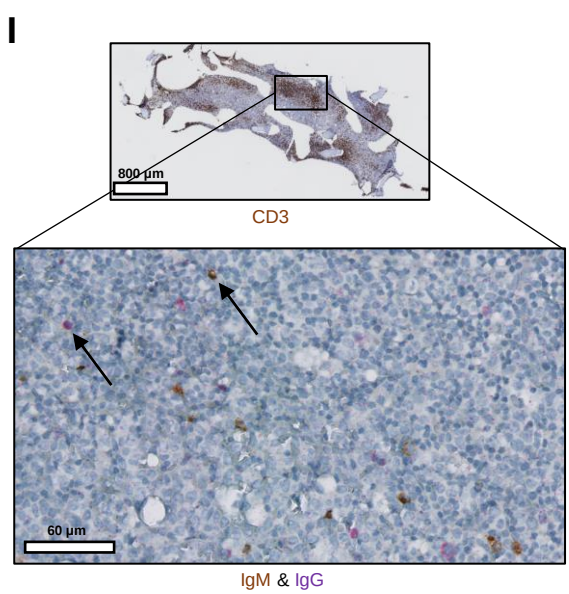
I
800 µm
CD3
60 µm
IgM & IgG

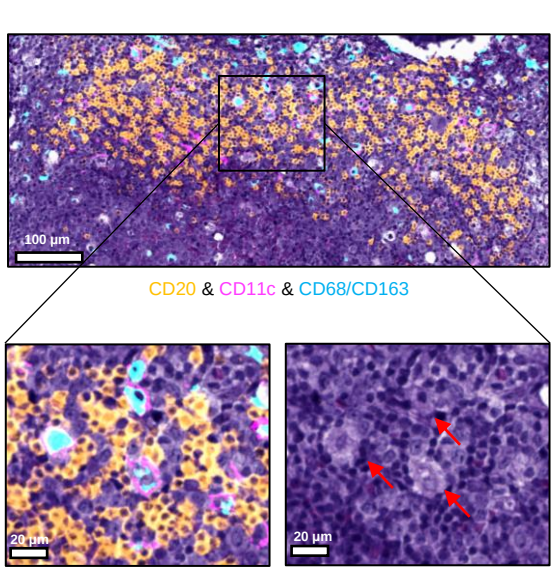
M
100 µm
CD20 & CD11c & CD68/CD163
20 µm
20 µm

Extended Data Figure 1

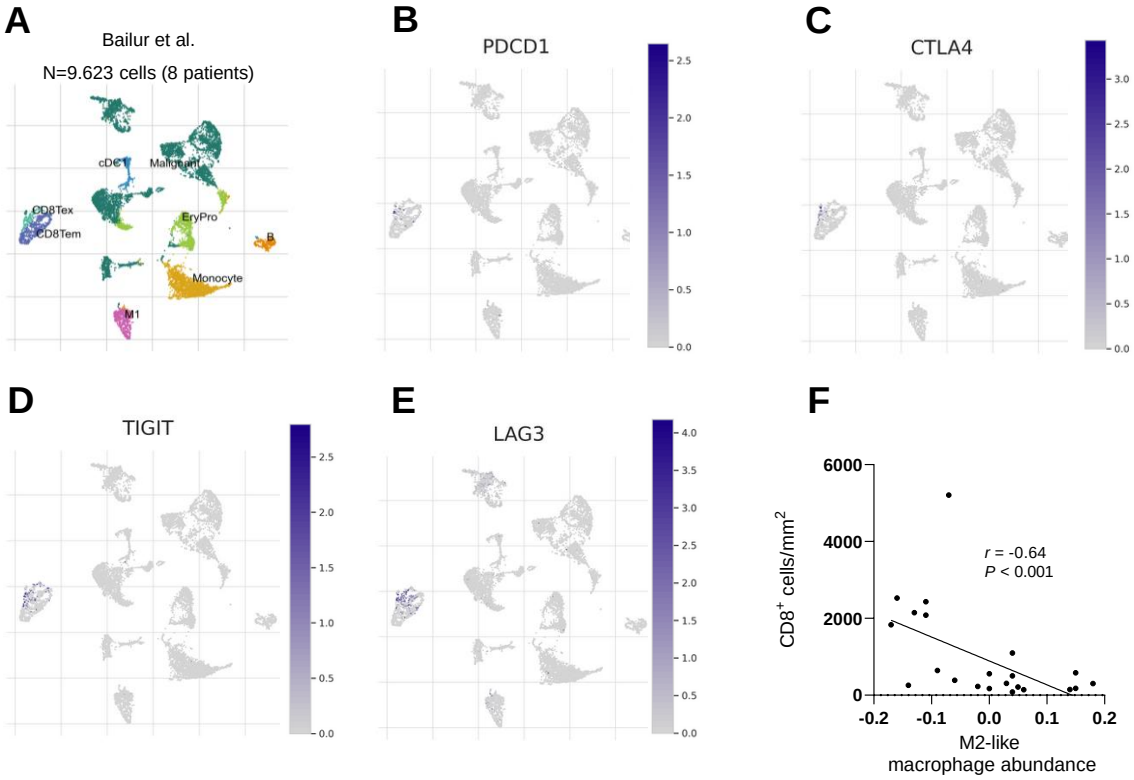
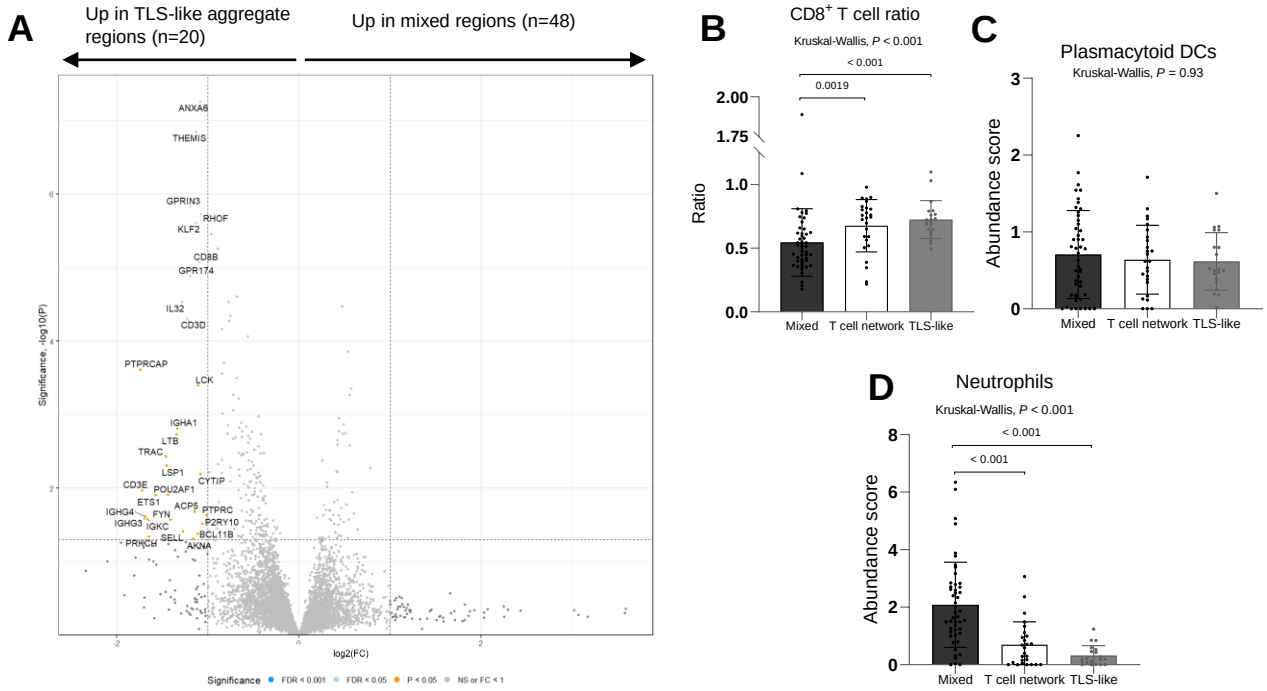
Extended Data Figure 2